nature nanotechnology

Letter https://doi.org/10.1038/s41565-022-01314-x

Electrical switching of a bistable moiré superconductor

In the format provided by the authors and unedited

CONTENTS

I. Crystallographic alignment of BN flakes

II. Additional transport data

III. Hysteretic MATBG Device 2

References

I. CRYSTALLOGRAPHIC ALIGNMENT OF BN FLAKES

During van der Waals assembly, the long crystallographic edges of the top and bottom BN flakes were aligned to each other. These edges are typically zigzag or armchair terminations of the lattice. Therefore, the edges are known modulo 30°. In Fig. S1, an optical microscope image of the final heterostructure is shown after removal of polycarbonate residues with a chloroform soak. The extracted relative BN alignment angle is $1.4 \pm 0.1°$ (modulo 30°). In order to minimize relaxation of the moiré heterostructures, no heat annealing steps were performed post-transfer.

Our device displays the same hysteresis direction as the reported device ('Device H2') of Ref. [1] consisting of AB-stacked bilayer graphene with its crystallographic axis aligned to the two BN axes. Second-harmonic generation (SHG) experiments reveal that their two BN crystals are at a 30° angle to one another (modulo 60°), in contrast to the reversed hysteresis direction for a different device with 0° alignment (modulo 60°). On this basis, we hypothesize that our MATBG device also has relative BN alignment of 30°.

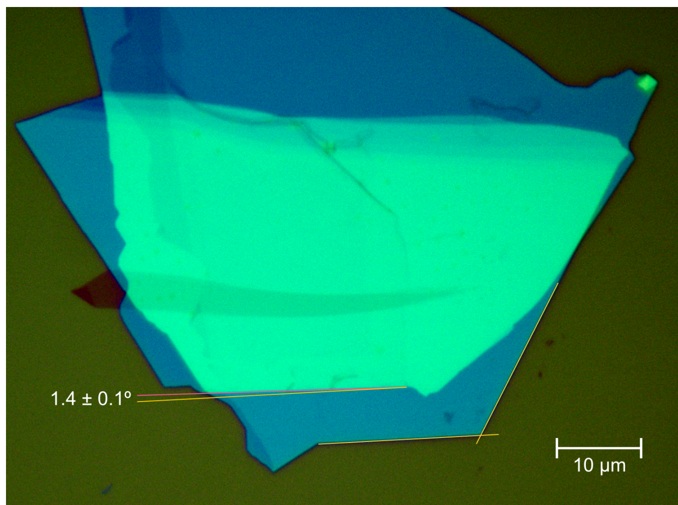

FIG. S1. **Alignment of BN flakes.** Optical microscope image showing crystallographic axes of top and bottom BN flakes of the stack. The relative angle between long edges is $1.4 \pm 0.1°$.

II. ADDITIONAL TRANSPORT DATA

We plot the four-probe longitudinal (R_{xx}) and transverse (R_{xy}) resistances in Fig. S2 and Fig. S3. In Fig. S2, we show these measurements at zero magnetic field after first polarizing the device at ±1 Tesla. Both measurements were taken with an AC excitation current of 10 nA and at a mixing chamber temperature of 65 mK. We observe no evidence at 0 Tesla of magnetic hysteresis that is characteristic of anomalous Hall behavior, which has previously been observed in single-BN-aligned MATBG devices near $\nu = 3$ [2, 3]. Furthermore, we also plot R_{xx} and R_{xy} at finite magnetic fields in Fig. S3. For each trace, R_{xx} and R_{xy} were symmetrized and antisymmetrized, respectively, using the following relations:

$$R_{xx}(B) = (R_{xx}(B) + R_{xx}(-B))/2 \tag{1}$$

$$R_{xy}(B) = (R_{xy}(B) - R_{xy}(-B))/2 \tag{2}$$

These measurements were performed with an AC excitation current of 1 nA and at a mixing chamber temperature of 300 mK. Here, we took careful care to use a small excitation current to avoid current-induced switching of a possible magnetic state. Again, there is no evidence of anomalous Hall behavior near $\nu = 3$.

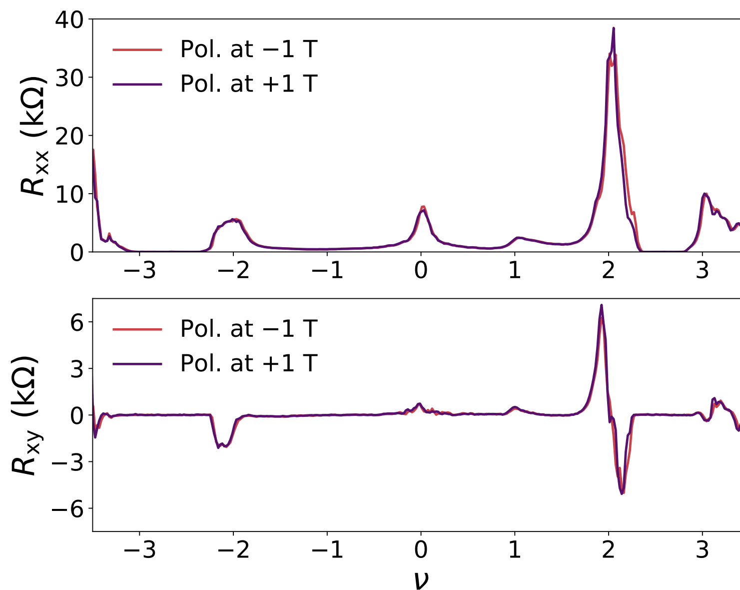

FIG. S2. **Longitudinal and transverse resistances at zero magnetic field.** Four-probe longitudinal R_{xx} and transverse R_{xy} resistances vs. filling factor ν using the bottom gate V_{BG}. A magnetic field of ±1 Tesla was applied prior to sweeping down to 0 Tesla for each measurement.

Fig. S4 shows the zoomed-in temperature dependence of four-probe longitudinal resistance R_{xx} measurements around the hole (Fig. S4a) and electron (Fig. S4b) superconducting domes. The back gate V_{BG} was used to tune the carrier density in one of the two bistable states. Vertical linecuts of R_{xx} vs. T for different filling factors ν are plotted for the hole (Fig. S4c) and electron (Fig. S4d) regions. To extract the critical temperatures T_{c}, first the normal state resistance R_{N} was fit to the equation $R_{\mathrm{N}}(T) = aT + b$ at higher temperatures. Then, T_{c} was extracted from the intersection of the data with xR_{N} for $x = 0.5$, 0.4, and 0.3 for 50%, 40%, and 30% of R_{N}, respectively. On the hole side, the maximal T_{c} occurs at $\nu = -2.62$ with $T_{\mathrm{c},50\%} = 2.15$ K, $T_{\mathrm{c},40\%} = 1.88$ K, and $T_{\mathrm{c},30\%} = 1.68$ K. The electron side has weaker superconductivity where the maximal T_{c} occurs at $\nu = 2.32$ with $T_{\mathrm{c},50\%} = 0.83$ K, $T_{\mathrm{c},40\%} = 0.79$ K, and $T_{\mathrm{c},30\%} = 0.74$ K.

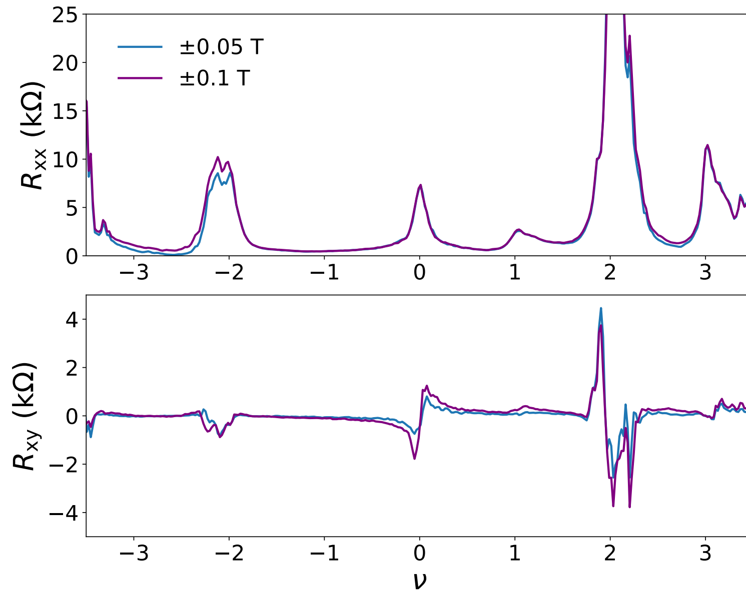

FIG. S3. **Longitudinal and transverse resistances at finite magnetic field.** Four-probe longitudinal R_{xx} (symmetrized) and transverse R_{xy} (antisymmetrized) resistances vs. filling factor ν (using the bottom gate V_{BG}) at small, finite applied mangetic fields.

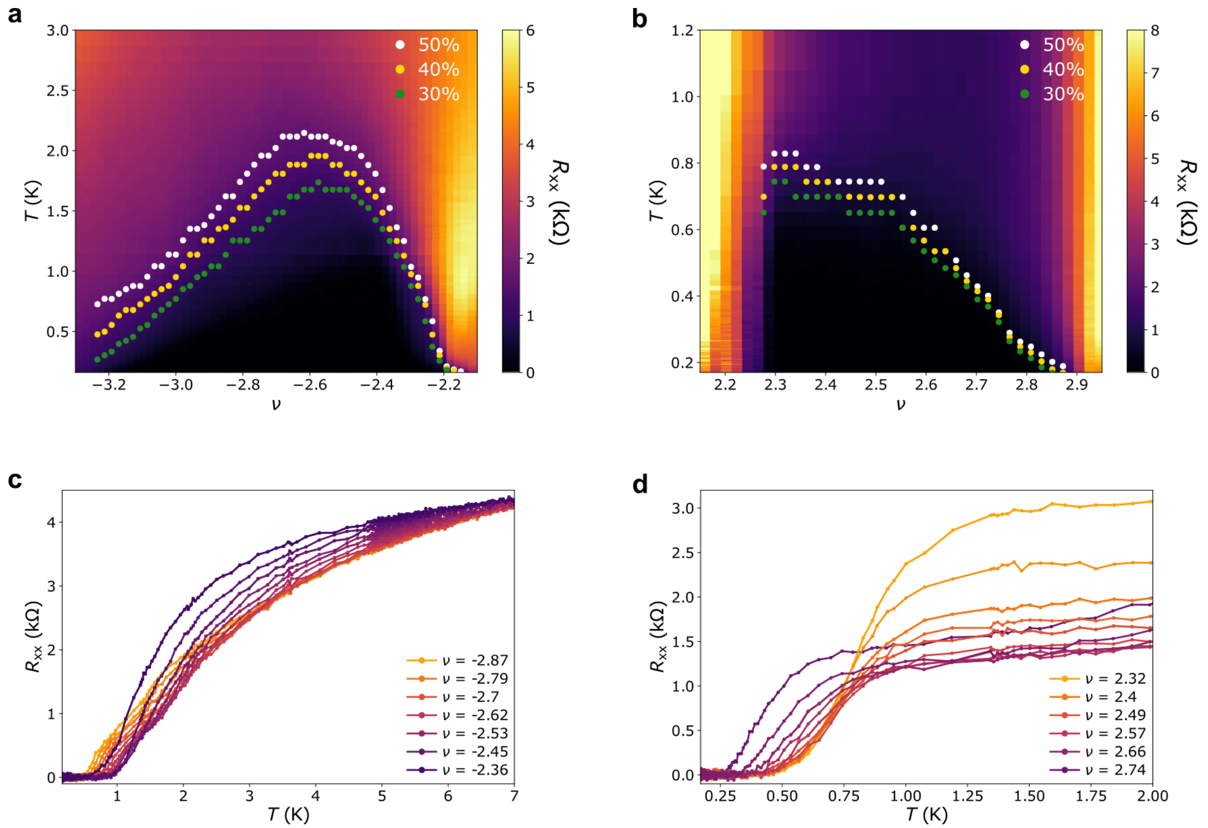

FIG. S4. **Temperature dependence of superconductivity. (a,b)** Four-probe longitudinal resistance R_{xx} vs. bottom gate V_{BG} and temperature for the hole and electron superconducting domes. The circles denote T_{c} extracted from 50%, 40%, and 30% of R_{N}. **(c,d)** Vertical linecuts of R_{xx} vs. T from **(a,b)** at different ν.

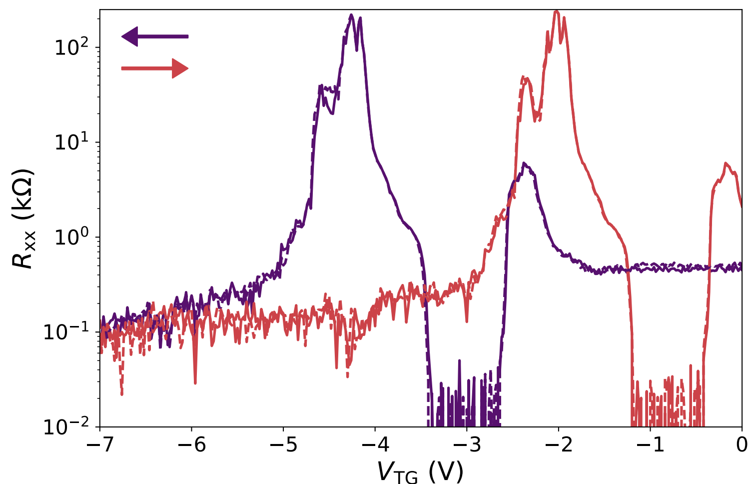

FIG. S5. **Bistability over time.** Four-probe longitudinal resistance R_{xx} versus top gate V_{TG}. First, the gate was swept down (solid purple) from 0 to −7 V and then up (solid pink) back to 0 V. These two scans were then repeated after waiting for 16 hours (dashed lines). The measurements were performed at 65 mK with an AC excitation current of 1 nA.

III. HYSTERETIC MATBG DEVICE 2

In addition to the device presented in the main text (Device 1), we fabricated a second MATBG device with aligned top and bottom BN flakes. In this case, the crystallographic edges of the two graphene layers were also closely aligned to the BN flakes (Fig. S6). The top and bottom BN edges are aligned by $0.5\pm0.1°$ (modulo 30°), and the top BN and top monolayer graphene flake in the MATBG stack are aligned by $0.3\pm0.1°$ (modulo 30°). Based on these rotations from optical microscopy and the MATBG twist angle of 0.99° extracted from transport measurements (see below), the bottom BN and bottom monolayer graphene flakes are also closely aligned near $1.8\pm0.2°$.

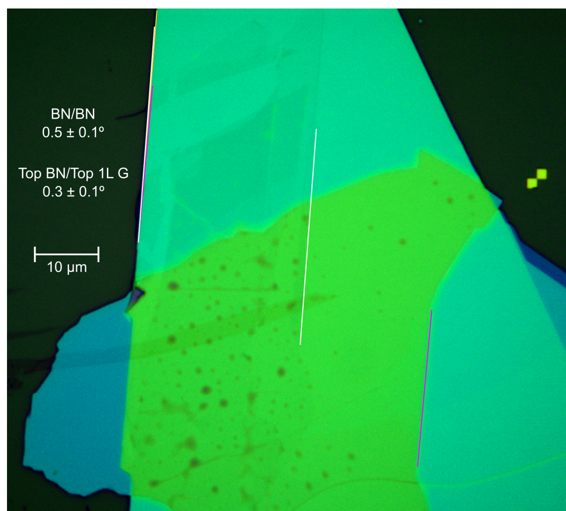

FIG. S6. **Flake alignment in Device 2.** Optical microscope image showing the angle alignment in a second hysteretic MATBG device. The crystallographic edges of the top (gold) and bottom (purple) BN flakes and the top monolayer graphene (white) are highlighted.

Upon sweeping the back gate V_{BG} at a temperature of 4.3 K (Fig. S7a), we observe a sharp charge neutrality peak ($\nu = 0$) and broad correlated insulator peaks at $\nu = 2$ and 3 in the four-probe longitudinal resistance R_{xx}. Using the positions of $\nu = 0$ and 3, we extract an MATBG twist angle of 0.99°.

Similarly to Device 1, the resistance is strongly dependent on sweep direction of the top gate V_{TG} (Fig. S7b). At first, the gate does not appear to inject carriers into MATBG, and then begins to work as a normal field-effect

transistor. This hysteresis direction also matches that of Device 1.

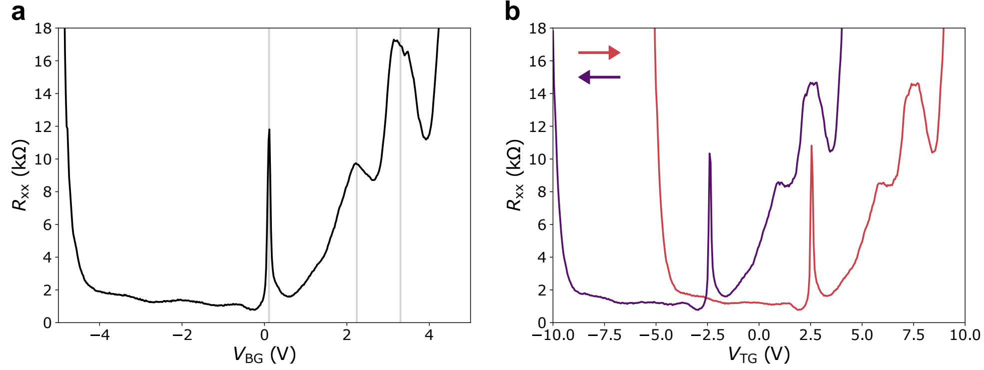

FIG. S7. **Top and bottom gate sweeps of Device 2.** **(a)** Four-probe longitudinal resistance R_{xx} as a function of bottom gate V_{BG}. Insulating peaks at $\nu = 0$, 2, and 3 are indicated by the grey vertical lines. **(b)** R_{xx} as a function of top gate V_{TG} when the gate is swept up (pink) and down (purple).

Dual-gate R_{xx} maps in Figs. S8a and S8b further demonstrate the hysteretic behavior of Device 2. In both cases, V_{BG} is swept up as the fast axis. The insulating transport features of R_{xx} when the slow axis V_{TG} is initially swept up (Fig. S8a) or down (Fig. S8b) are independent of V_{TG} until a critical threshold is reached. Beyond this point, the top gate acts normally, characterized by straight-line insulating peaks in the V_{BG}-V_{TG} plane. This behavior can also be visualized in the n_{ext}-D_{ext} plane (Fig. S8c and S8d), as was done for Device 1, using the definitions: $n_{ext} = (\varepsilon_{BN}/e)(V_{TG}/d_{TG} + V_{BG}/d_{BG})$, $D_{ext}/\varepsilon_0 = (\varepsilon_{BN}/2)(V_{TG}/d_{TG} - V_{BG}/d_{BG})$.

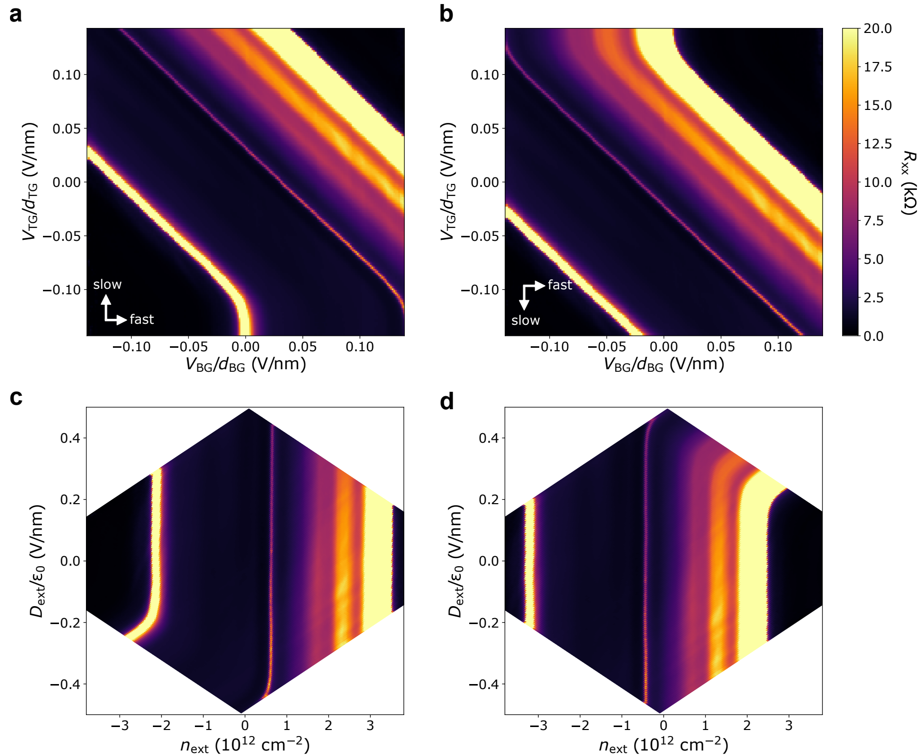

FIG. S8. **Dual-gate maps of longitudinal resistance.** **(a, b)** Four-probe longitudinal resistance R_{xx} vs. top gate V_{TG} and bottom gate V_{BG}. The fast scan axis is V_{BG}, swept up from negative to positive. The slow scan axis is V_{TG}, swept up in **(a)** and down in V_{TG}. Axes are normalized to the BN dielectric thicknesses of the two gates. **(c, d)** Converted maps of **(a, b)** in units of n_{ext} and D_{ext}/ε_0 (see text).

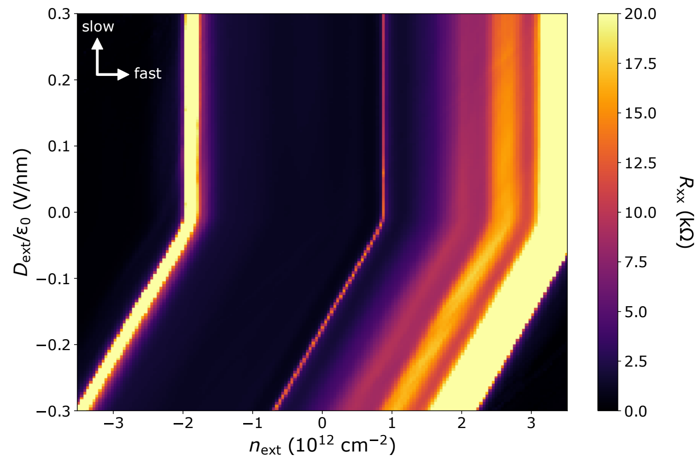

FIG. S9. **Evolution of R_{xx} with applied carrier density and displacement field.** Four-probe longitudinal resistance R_{xx} vs. n_{ext} and D_{ext}, as defined in the text from V_{TG} and V_{BG}. The fast scan axis is n_{ext} and the slow scan axis is D_{ext}.

In Device 2, we also performed measurements in which we swept n_{ext} and D_{ext} as the fast and slow axes, respectively (Fig. S9). Initially, at large negative D_{ext}, the resistive features of MATBG appear to evolve with the defined D_{ext}. At a certain value of D_{ext}, however, the system abruptly changes and the correlated states of MATBG are completely independent of D_{ext}, as expected for an MATBG device without hysteretic gate behavior.

[1] Z. Zheng, Q. Ma, Z. Bi, S. de la Barrera, M.-H. Liu, N. Mao, Y. Zhang, N. Kiper, K. Watanabe, T. Taniguchi, J. Kong, W. A. Tisdale, R. Ashoori, N. Gedik, L. Fu, S.-Y. Xu, and P. Jarillo-Herrero. Unconventional ferroelectricity in moiré heterostructures. *Nature*, 588:71–76, 2020.

[2] A. L. Sharpe, E. J. Fox, A. W. Barnard, J. Finney, K. Watanabe, T. Taniguchi, M. A. Kastner, and D. Goldhaber-Gordon. Emergent ferromagnetism near three-quarters filling in twisted bilayer graphene. *Science*, 365:605–608, 2019.

[3] M. Serlin, C. L. Tschirhart, H. Polshyn, Y. Zhang, J. Zhu, K. Watanabe, T. Taniguchi, L. Balents, and A. F. Young. Intrinsic quantized anomalous Hall effect in a moiré heterostructure. *Science*, 367:900–903, 2020.